Four Dimensional Image Registration For Intravital Microscopy

Chichen Fu
Purdue University
West Lafayette, Indiana

Neeraj Gadgil
Purdue University
West Lafayette, Indiana

Khalid K. Tahboub
Purdue University
West Lafayette, Indiana

Paul Salama
Indiana University-Purdue University
Indianapolis, Indiana

Kenneth W. Dunn
Indiana University
Indianapolis, Indiana

Edward J. Delp
Purdue University
West Lafayette, Indiana

Abstract

Increasingly the behavior of living systems is being evaluated using intravital microscopy since it provides subcellular resolution of biological processes in an intact living organism. Intravital microscopy images are frequently confounded by motion resulting from animal respiration and heartbeat. In this paper we describe an image registration method capable of correcting motion artifacts in three dimensional fluorescence microscopy images collected over time. Our method uses 3D B-Spline non-rigid registration using a coarse-to-fine strategy to register stacks of images collected at different time intervals and 4D rigid registration to register 3D volumes over time. The results show that our proposed method has the ability of correcting global motion artifacts of sample tissues in four dimensional space, thereby revealing the motility of individual cells in the tissue.

1. Introduction

Recent advances in intravital microscopy allow imaging biological processes as they occur in living animals [1, 2, 3]. Intravital microscopy has been particularly useful for studies of the immune system [4, 5]. An effective immune response depends upon the behavior of immune cells, whose actions result in a defensive response against pathogens such as bacteria or viruses. Intravital microscopy is uniquely capable of characterizing the migration, activity and interactions of immune cells, making it a powerful tool for understanding the immune function. Studies of immune cell motility typically involve acquiring images of a 3D volume of tissue collected over time. Cell tracking is then used to characterize and quantify the motility of fluorescently-labeled immune cells in the tissue volume. The ability to characterize cell motility within a volume of tissue in a liv-

ing animal is frequently compromised by global movement of the tissue resulting from animal respiration and heartbeat. Global motion artifacts must be corrected before cell tracking using image registration [6].

For microscopy, image registration focuses on aligning images from different focal slices and images or volumes taken from different times. In general, the most frequently used registration techniques can be divided into two categories. Intensity-based registration and feature-based registration [6, 7].

Feature-based methods comprise the use of image features used for feature correspondence matching and the estimation of an affine transformation matrix that corresponds to the distortion [6, 7]. The main difficulties of feature-based registration include choosing the features and matching them across the images. Specifically, for images that contain highly active live cells that are traveling in 3D space, feature selection and matching can be challenging. Feature-based methods have better performance when similar structures are present in the scene.

A point-based 3D registration method that cancels 3D global translations and rotation around the z-axis in microscopy images with live cells is described in [8]. It uses threshold-based features, a feature matching method described in [9], and least-squares estimation of the affine transformation. This method is computationally fast because it uses partial information within the images but fails when there are significant scene changes. In [10], 4D microscopy images are registered by (i) matching Z directional image slices at different time volumes to find Z direction translation and (ii) using 2D landmark-based feature matching to align temporal volumes in the X and Y directions.

Intensity-based registration methods are often associated with deformation models, affine transformations, search methods, and similarity metrics. Many rigid and non-rigid intensity-based registration methods have been developed

using deformation models, search methods, and similarity metrics. In [11], a non-rigid registration method that minimizes residual complexity is described. Many similarity metrics such as sum of squared difference (SSD), gradient differences (GD), gradient correlation (GC), pattern intensity (PI), and mutual information (MI) [12, 13] have been used. GD and GC are gradient based methods that work well on the images with significant gradient information. MI is an entropy related method that has been effectively used on MRI and PET images, PI requires high contrast of input images to achieve high performance [12], and SSD can work effectively under more relaxed constraints and with less computational cost.

A voxel-based rigid registration method is described in [14] that uses modified Marquardt-Levenberg optimization with a coarse-to-fine strategy to register 2D images or 3D volumes. This method produces promising results with functional magnetic resonance imaging (fMRI) and intramodality positron emission tomography (PET) data, which are different from microscopy images in that fMRI and PET images usually contain well defined structures.

A non-rigid registration method that utilizes multi-channel temporal 2D and 3D microscopy images of cell nuclei to address global rigid and local non-rigid motion artifacts of cell nuclei is described in [15]. Another rigid registration method for canceling motion artifacts of biological objects based on frequency domain techniques is described in [16]. Yet another non-rigid registration method [17] that cancels motion artifacts of subcellular particles in live cell nuclei in temporal 2D and 3D microscopy images by using the extensions of an optic flow method. However, these techniques [15, 16, 17] are mainly used to register images that contain single cellular structure. An thin plate spline non-rigid registration method that registers images containing many live cells is described in [18], but it can only cancel the motion artifacts between successive z stack images.

One of the objectives of our work in general is to track live cells while preserving functional motion. In general, non-rigid registration techniques have the ability to correct local object motion, but may "over register" and distort biological functional motion. Rigid registration techniques alternatively can preserve the cell motion and also cancel global motion artifacts. The images used in this paper consists of a time series of four-channel (spectral channels red, green, blue, and yellow) 3D fluorescence microscopy volumes of immune cells collected from a mouse kidney. To be clear, our dataset consists of 4 spectral channels, each spectral channel is a 3D volume and the 3D volumes for each spectral channel are acquired over time at regular time intervals. We have 61 time samples where each time sample consists of 4 spectral channels. For each spectral channel we have 11 focal slices in the z direction (depth) where each focal slice is 512×512 pixels. The focal slices are acquired

serially. Three spectral channels of the dataset contain immune cells that are moving in 3D space over time and the other spectral channel contains relatively stable blood flow through a tubular shaped structure. The cells are highly active over time and motion artifacts can be observed. Since the biological functional motion of the cells is valuable, cell motion over time should be preserved after registration. As we describe below, we consider our registration problem as a combination of two registration problems, a 3D non-rigid registration and 4D rigid registration. The 3D non-rigid registration focuses on canceling motion artifacts between focal slices at different time volumes and the 4D rigid registration focuses on canceling motion artifacts between time volumes.
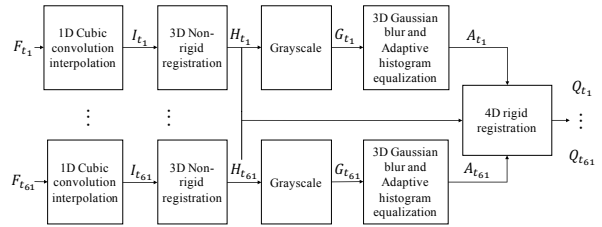
2. Proposed Method

Figure 1. Block diagram of our proposed method

Figure 1 shows the block diagram of our proposed method. Our method consists of 1D cubic convolution interpolation, 3D non-rigid registration, 3D Gaussian blur, adaptive histogram equalization, and 4D rigid registration.

Throughout the paper, we use the following notation to represent the images, $F_{t_n, b_m}^{z_q}$, where z_q, t_n, b_m represent focal slices (z dimension), time samples, and spectral channels, respectively, where $q \in \{1, 2, \ldots, 11\}$, $n \in \{1, 2, \ldots, 61\}$, and $m \in \{1, 2, 3, 4\}$. The four channels 3D volume at the nth time sample in $F_{t_n, b_m}^{z_q}$ is denoted by F_{t_n}. For example, $F_{t_1, b_2}^{z_5}$ is the 512×512 pixel image representing the second spectral channel at the first time sample and the 5th focal slice within the volume. F_{t_1} contains 3D volumes from the four spectral channels collected at the first time sample with each volume consisting of 11 slices of 512×512 pixel images. Similarly, $I_{t_n, b_m}^{z_q}$, $H_{t_n, b_m}^{z_q}$, $Q_{t_n, b_m}^{z_q}$ denote the result of 1D cubic convolution interpolation, the result of 3D non-rigid registration, and the final 4D registration output, such that $q \in \{1, 2, \ldots, 41\}$, $n \in \{1, 2, \ldots, 61\}$, and $m \in \{1, 2, 3, 4\}$ (see Figure 1). The result of the 3D Gaussian blur and adaptive histogram equalization is denoted by $A_{t_n}^{z_q}$, such that $q \in \{1, 2, \ldots, 41\}$, and $n \in \{1, 2, \ldots, 61\}$. $A_{t_n}^{z_q}$ is a grayscale image. Please note that the total number of focal slices (as indicated by q) for $I_{t_n, b_m}^{z_q}$, $H_{t_n, b_m}^{z_q}$, $Q_{t_n, b_m}^{z_q}$ is 41 compared to 11 for

$F_{t_n,b_m}^{z_q}$ since we use interpolation as described below. We mentioned above we register our images using 3D non-rigid registration and 4D rigid registration. F_{t_n} is up-sampled in the z direction to increase the resolution, the results is I_{t_n}. 3D non-rigid registration is then used to register z slices for each channel of a 3D volume at different time samples. The result is H_{t_n} is first transformed to grayscale images and then enhanced by using a 3D Gaussian blur and adaptive histogram equalization. 4D registration is used to estimate rigid body affine transformations for aligning A_{t_n}. The estimated affine transformations are then used to map H_{t_n} to the final result, Q_{t_n}, which are aligned in both time and the z direction.

2.1. Interpolation and 3D Non-Rigid Registration

To smooth our data, cubic convolution interpolation is used as a pre-processing step [19]. We up sample $F_{t_n,b_m}^{z_q}$ in the z direction by a factor of 4 to obtain $I_{t_n,b_m}^{z_q}$. Up sampling is done by inserting three data points between every two adjacent pixels in an image to produce 41 interpolated images for each spectral channel and time sample.

3D non-rigid registration is then used in the z direction to align the focal slices at each time sample. We use the non-rigid method described in our previous work [20, 21] because this method can effectively eliminate 3D non-rigid motion artifacts between focal slices. This technique initially starts with a rigid registration step and then uses localized non-rigid registration. The four spectral channels are transformed to grayscale images using the spectral channel weights described in [20, 21]. First, rigid registration is used to reduce global motion artifacts between images. This rigid registration uses Limited Memory Broyden-Fletcher-Goldfarb-Shanno (L-BFGS) Quasi-Newton optimization [22] to estimate the rigid body affine transformation. A localized non-rigid B-spline registration is then done on the results of the rigid registration described above to cancel the local non-rigid motion artifacts[20, 21].

In order to cancel the local non-rigid motion artifacts, images are deformed by establishing meshes of control points. A transformation is estimated to account for the movement of deformation fields using B-splines with L-BFGS Quasi-Newton optimization. A grid of control points is used in our method with 64 pixels spacings in X and Y directions.

2.2. Four Dimensional Rigid Registration

Having corrected motion artifacts between different focal planes, we use rigid registration to correct global translations and rotations. The input to this step is a set of multi-channel temporal 3D non-rigid registered volumes H_{t_n}. The multi-channel dataset used in this paper contained four channels: red, green, blue, and yellow. First, we transform the images in each time volume to composite grayscale im-

ages using a weighted sum:

$$G_{t_n} = \sum_{i=1}^{4} \frac{\bar{H}_{t_n,b_i}}{\sum_{j=1}^{4} \bar{H}_{t_n,b_j}} H_{t_n,b_i} \qquad (1)$$

where $H_{t_n,b_i}, i \in \{1,2,3,4\}$ are the nth red channel, green channel, blue channel, and yellow channel 3D volumes, respectively. $\bar{H}_{t_n,b_i}, i \in \{1,2,3,4\}$ are the averaged pixel values of these channel volumes, respectively and G_{t_n} is the nth composite grayscale volume.

Biological structures are usually poorly defined in microscopy images. In order to create better defined structures, to improve registration performance, the grayscale images are 3D Gaussian blurred. Since our registration method is image intensity-based, low intensity and low contrast of the original images tend to cause the optimization method to be trapped in local minima, consequently producing incorrect affine transformation in intensity-based registration. To address this we enhance the grayscale images using adaptive histogram equalization (AHE) after the 3D Gaussian blur.

Affine transformations are then used between adjacent time volumes to minimize motion artifacts. The affine transformations are restricted to translations and rotations since we only focus on canceling rigid body motion artifacts at this stage. Denoting the translations and rotations in the X, Y, and Z directions, by $(t_x, t_y, t_z, \theta_x, \theta_y, \theta_z)$ respectively, the corresponding translation and rotation matrices are given in Equations (2 - 6):

$$R_x = \begin{bmatrix} 1 & 0 & 0 & 0 \\ 0 & \cos(\theta_x) & -\sin(\theta_x) & 0 \\ 0 & \sin(\theta_x) & \cos(\theta_x) & 0 \\ 0 & 0 & 0 & 1 \end{bmatrix} \qquad (2)$$

$$R_y = \begin{bmatrix} \cos(\theta_y) & 0 & \sin(\theta_y) & 0 \\ 0 & 1 & 0 & 0 \\ -\sin(\theta_y) & 0 & \cos(\theta_y) & 0 \\ 0 & 0 & 0 & 1 \end{bmatrix} \qquad (3)$$

$$R_z = \begin{bmatrix} \cos(\theta_z) & \sin(\theta_z) & 0 & 0 \\ -\sin(\theta_z) & \cos(\theta_z) & 0 & 0 \\ 0 & 0 & 1 & 0 \\ 0 & 0 & 0 & 1 \end{bmatrix} \qquad (4)$$

$$T = \begin{bmatrix} 1 & 0 & 0 & t_x \\ 0 & 1 & 0 & t_y \\ 0 & 0 & 1 & t_z \\ 0 & 0 & 0 & 1 \end{bmatrix} \qquad (5)$$

$$M = R_x R_y R_z T \qquad (6)$$

where R_x, R_y, R_z denote the rotation matrices around the X, Y, and Z axis respectively, T the translation matrix, and M the final affine transformation.

Broyden-Fletcher-Goldfarb-Shanno (BFGS) Quasi-Newton optimization was used to estimate the parameters $m(t_x, t_y, t_z, \theta_x, \theta_y, \theta_z)$ by minimizing the sum of the squared differences (SSD) between different time volumes [23, 24, 25, 26]. The optimal transformation is given by Equation (7):

$$M_n = \min_{M'} \sum_{x,y,z} [f(M', A_{t_n})(x, y, z) \\ - A_{t_{n-1}}(x, y, z)]^2 \tag{7}$$

where A_{t_n} is the nth moving volume to be registered, $A_{t_{n-1}}$ the reference volume, $f(M', A_{t_n})$ the mapping that transforms current volume A_{t_n} by using transformation matrix M', and (x, y, z) are pixel coordinates.

When estimating the parameters of the affine transformation, we separate the process into two steps. First we estimate (t_x, t_y, θ_z) and $(\theta_x, \theta_y, t_z)$ separately with initial values of $(0, 0, 0)$. Second, we use the result from the previous step as an initial point of the final stage to obtain $(t_x, t_y, t_z, \theta_x, \theta_y, \theta_z)$. We have observed that using this strategy produces better results than doing the estimation in one step. Let M_i be the transformation estimated using the current time volume A_{t_i} and previous time volume $A_{t_{i-1}}$, and let T_n be the final affine transformation needed to correct motion artifacts between time volumes A_{t_1} and A_{t_n}. T_n is given by:

$$T_n = M_1 \times M_2 \times \cdots \times M_n \tag{8}$$

After the affine transformations of all the time volumes are estimated, the final registration outcomes are obtained by Equation 9:

$$Q_{t_n} = f(T_n, H_{t_n}) \tag{9}$$

where Q_{t_n} is the nth registered time volume. 3D cubic interpolation is used to transform pixels with non-integer coordinates in the function $f(\cdot)$. The registered volume's final size is the sum of the size of original volume and the maximum distance between original pixel locations and the transformed pixel coordinates in each direction.

2.3. 3D Motion Vector Estimation - Validation

Validation of microscopy image registration can be daunting since ground-truth information is difficult to obtain on large image volumes. Block-matching is used to estimate motion vectors between the reference time volume and current time volume. This is somewhat similar to block matching techniques used in video compression. The current time volume and reference time volume are equally divided into blocks (sub-volumes). Each block in the current volume is matched with the corresponding adjacent blocks in the reference volume. Motion vectors are created to record the motion of corresponding blocks

in the reference volume and the current volume that are matched. 3D time volumes are divided into sub-volumes with the size of i × j × k. A search window with the size of $(2p + 1) \times (2p + 1) \times p_z$ is created by setting the search range in the x,y, and z directions to (p, p, p_z).

To find the matching blocks and 3D motion vector $v = (i, j, k)$, the sum of absolute difference between reference block and current searching block is used:

$$v = \min_{a,b,c} \sum_{m,n,l} |Q_{t_n}(x + m + a, y + n + b, z + l + c) \\ - Q_{t_{n-1}}(x + m, y + n, z + l)| \tag{10}$$

where $Q_{t_n}(x + m + a, y + n + b, z + l + c)$ is the current searching block in time volume Q_{t_n} centered at $(x + a, y + b, z + c)$, $Q_{t_{n-1}}(x + m, y + n, z + l)$ is the reference block centered at (x, y, z) in time volume $Q_{t_{n-1}}$, and (a, b, c) is the motion vector to be estimated. After the motion vectors are obtained, we create a 3D spherical histogram of the motion vectors with 36×36 bins to quantify the motion results.

3. Experimental Results

The images used in the experiments consists of a time series of four-channel (spectral channels red, green, blue, and yellow) 3D fluorescence microscopy volumes of immune cells collected from a mouse kidney. To be clear, our dataset consists of 4 spectral channels, each spectral channel is a 3D volume and the 3D volumes for each spectral channel are acquired over time at regular time intervals Samples of the four spectral channels are shown in Figure 2.
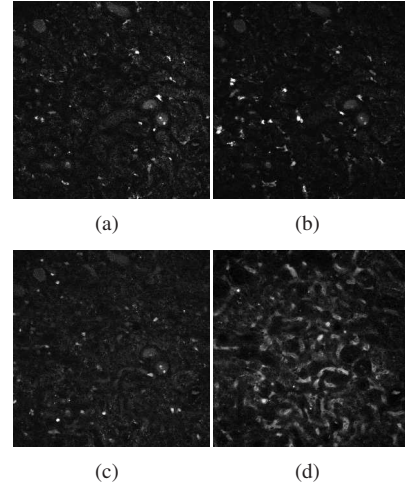

(a)   (b)

(c)   (d)

Figure 2. Grayscale versions of the four different spectral channels of the 6th focal slice of the 1st time volume of the original dataset. (a) Green channel, (b) Yellow channel, (c) Red channel, (d) Blue channel.

As shown in Figure 3, 1D cubic convolution interpolation is used to interpolate images in the z direction with the up-sampling factor of 4 in each 3D volume. Figure 3 (a) shows the YZ view of the green channel of an original 3D volume and the result of interpolation is shown in 3 (b). Note that the resulting 3D volume contains 4 times the number of images of the original.
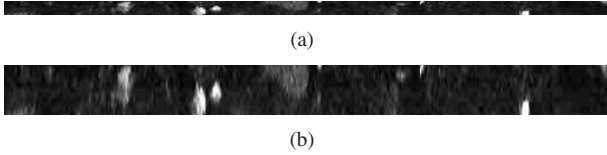

(a)

(b)

Figure 3. YZ view of the green channel of the original and the interpolated sample images. (a) Original, (b) Interpolated.

(a)   (b)

(c)   (d)

Figure 4. Sample images of our 3D non-rigid registration. (a) MIP of the sample original volume projected on XY plane, (b) MIP of the sample result of 3D non-rigid registration projected on XY plane, (c) MIP of the sample original volume projected on YZ plane, (d) MIP of the sample result of 3D non-rigid registration projected on YZ plane.
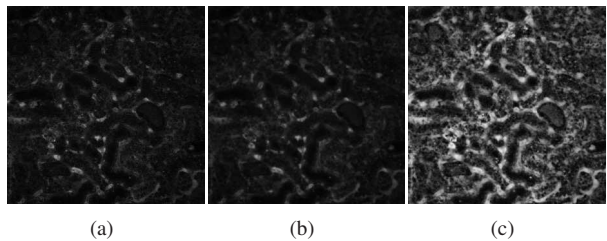

(a)   (b)   (c)

Figure 5. Sample results of pre-processing methods. (a) Composite grayscale original image, (b) 3D Gaussian blur, (c) Adaptive histogram equalization.

To evaluate the results of our registration method, we use maximum intensity projection (MIP) to project one 3D volume onto an image and many 3D volumes onto one 3D volume[20, 21]. The MIP of one 3D volume is obtained by selecting the maximum of all intensity values in one dimension (e.g. the z-direction or the time series) at each pixel location. The MIP of a 3D volume is used to show motion artifacts between focal slices, whereas the MIP of many 3D volumes representing different time samples is used to show motion artifacts between these volumes.

In Figure 4, we show the MIP of an original 3D volume and the MIP of the resulting 3D non-rigid registration. As we described in Section 2.1, 3D non-rigid registration is used to register focal slices within different 3D volumes. Since focal slices within different 3D volumes of our original dataset are well aligned initially, the impact of 3D non-rigid registration [20] can be observed in Figure 4. Temporal 3D microscopy data may not be well aligned in the z direction because all focal planes cannot be imaged at the same time instance. Therefore, 3D non-rigid registration is necessary to reduce motion artifacts between focal slices within different 3D volumes.

As shown in Figure 5 (a), the contrast of the four-channel composite sample image is very low and the biological structures are poorly defined. Therefore, a 3D Gaussian blur filter with $17 \times 17 \times 9$ rectangular window was used on the results of the 3D non-rigid registration followed by adaptive histogram equalization that employs $17 \times 17 \times 9$ rectangular window. Figure 5 (b) and (c) show the sample result of Gaussian blur and the sample result of adaptive histogram equalization. It can be observed that the sample image is enhanced.

Figure 6 (a) shows the MIPs projected on the XY plane of the original volumes at various samples. Figure 6 (c) shows the MIPs projected on the YZ plane. In Figure 6 (b) and (d), the MIPs of the results of our proposed 4D rigid registration method are shown. We also obtain the MIP of the entire 61 time volumes and use the ImageJ 3D viewer [27] to visualize it. Note that, this MIP is obtained by projecting a 4D volume on a 3D volume, whereas each of the MIPs shown in Figure 6 is obtained by projecting a 3D volume on a 2D image. The XY and YZ views of the MIP of the original time volumes are shown in Figure 7 (a) and (c) respectively. Figure 7 (b) and (d) show respectively the XY and YZ views of the MIP of the results of our proposed 4D rigid registration method. The MIP of original volumes appear to be smeared due to the global translations and rotations in time series. The MIP of registered volumes is sharper. The motility of cells can be observed in this MIP since it is a projection of the moving cells from different 3D volumes onto one volume. Note that the motions of cells are preserved during the registration process.

As shown in Figure 6 and Figure 7, our method successfully addressed the motion artifacts in our dataset and effectively cancel the motion artifacts in 4D space.
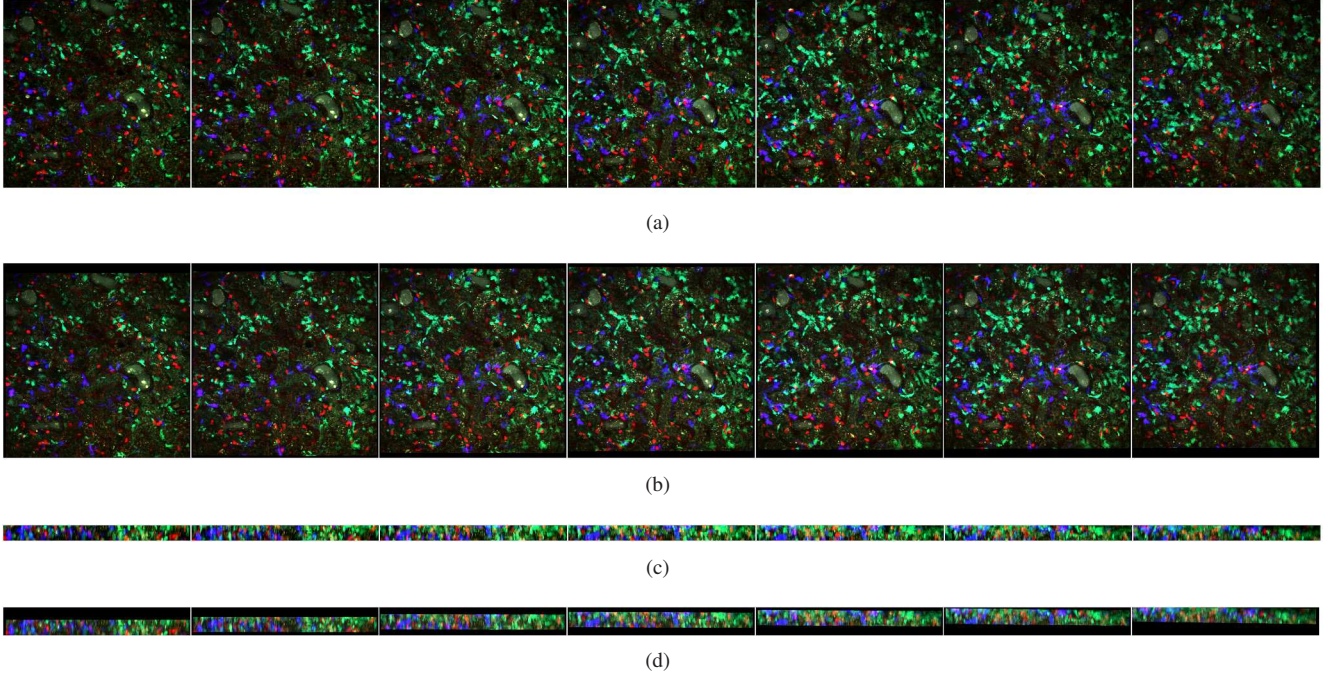
Figure 6. MIPs of the original time volumes and registered time volumes at time sample 1,11,21,31,41,51, and 61. (a) MIP of the original volumes projected on XY plane, (b) MIP of the result of 4D rigid registered volumes projected on XY plane, (c) MIP of the original volumes projected on YZ plane, (d) MIP of the result of 4D rigid registered volumes projected on YZ plane.

Time point #	Average SSD per pixel before registration	Average SSD per pixel after registration	Improvement percentage (%)
11	7.88	6.59	16.41
21	9.45	8.71	7.84
31	10.29	8.54	16.94
41	12.52	8.79	29.76
51	9.36	7.98	14.79
61	8.76	7.08	19.12

Table 1. Average SSD per pixel of different sample time volumes before and after registration and percentage of improvement.

The average sum of squared differences (SSD) per pixel of the original and registered volumes are shown in Table 1. The percentage improvement of the registered volumes as compared to the original is also shown. It can be observed that the average SSD per pixel decreases after 4D rigid registration indicating that the similarity between the reference and moving volumes is increased.

In addition, three dimensional motion vector analysis is used to validate the registration results as described in Section 2.3. Three dimensional motion vectors are obtained between adjacent time volumes using $(16, 16, 8)$ as block size and $(4, 4, 4)$ as search window. Three dimensional spherical histograms are shown in Figures 8 and 9 using 36×36 bins of directions, each bin has range of 10 degrees. Various views of the three dimensional spherical histograms are shown in Figures 8 and 9 to help visualize the results. We observe that estimated motion are significantly reduced.

4. Conclusions

This paper described a registration method to register 4D microscopy data consisting of time-lapse 3D volumes. We tested our method on multi-channel temporal 3D microscopy images that contains highly active cells. The results demonstrate that we can correct the motion artifacts and preserve the original motion of biological structures. In the future we will generalize our method to a 4D non-rigid registration technique that can cancel the non-rigid motion artifacts in temporal 3D images.
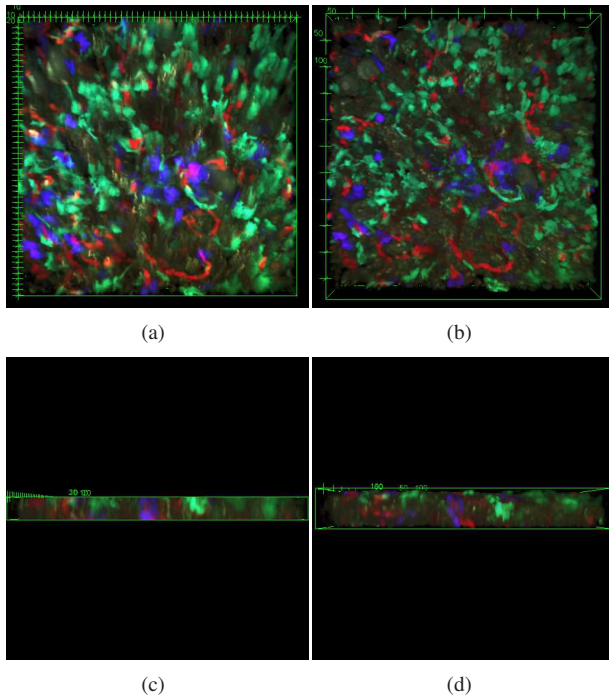
5. Acknowledgments

Figure 7. Views of MIP volumes (using ImageJ 3D viewer). (a) XY view of original MIP volume, (b) XY view of 4D rigid registered MIP volume, (c) YZ view of original MIP volume, (d) YZ view of 4D rigid registered MIP volume.

References

[1] K. W. Dunn, R. M. Sandoval, K. J. Kelly, P. C. Dagher, G. A. Tanner, S. J. Atkinson, R. L. Bacallao, and B. A. Molitoris, "Functional studies of the kidney of living animals using multicolor two-photon microscopy," *American Journal of Physiology - Cell Physiology*, vol. 283, no. 3, pp. C905–916, September 2002.

[2] W. Denk, J. H. Strickler, and W. W. Webb, "Two-photon laser scanning fluorescence microscopy," *Science*, vol. 248, no. 4951, pp. 73–76, April 1990.

[3] J. Peti-Peterdi, I. Toma, A. Sipos, and S. L. Vargas, "Multiphoton imaging of renal regulatory mechanisms," *Physiology*, vol. 24, no. 2, pp. 88–96, April 2009.

[4] C. Sumen, T. R. Mempel, I. B. Mazo, and U. H. von Andrian, "Intravital microscopy: visualizing immunity in context," *Immunity*, vol. 21, no. 3, pp. 315–329, September 2004.

[5] M. J. Hickey and P. Kubes, "Intravascular immunity: the host–pathogen encounter in blood vessels," *Nature Reviews Immunology*, vol. 9, no. 5, pp. 364–375, May 2009.

[6] L. Qu, F. Long, and H. Peng, "3-D registration of biological images and models: Registration of microscopic images and
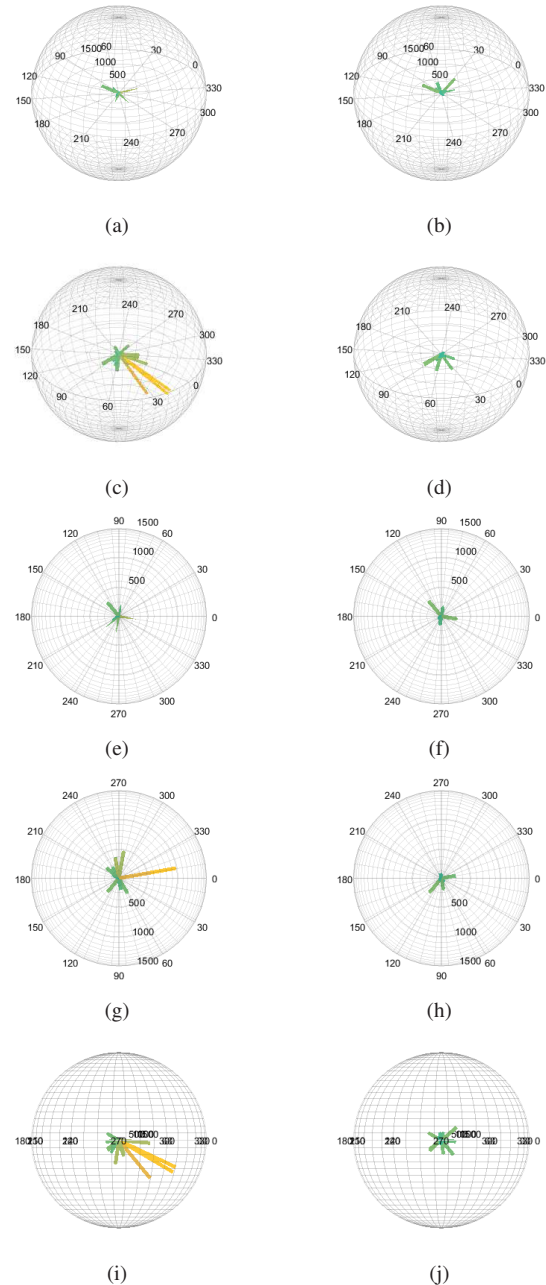

Figure 8. 3D spherical histograms of motion vectors using time volume 9 as the moving volume and time volume 8 as the reference volume. (a) histogram of original volume in the view from top, (b) histogram of registered volume in the view from top, (c) histogram of original volume in the view from bottom, (d) histogram of registered volume in the view from bottom, (e) histogram of original volume in +XY view, (f) histogram of registered volume in +XY view, (g) histogram of original volume in -XY view, (h) histogram of registered volume in -XY view, (i) histogram of original volume in XZ view, (j) histogram of registered volume in XZ view.
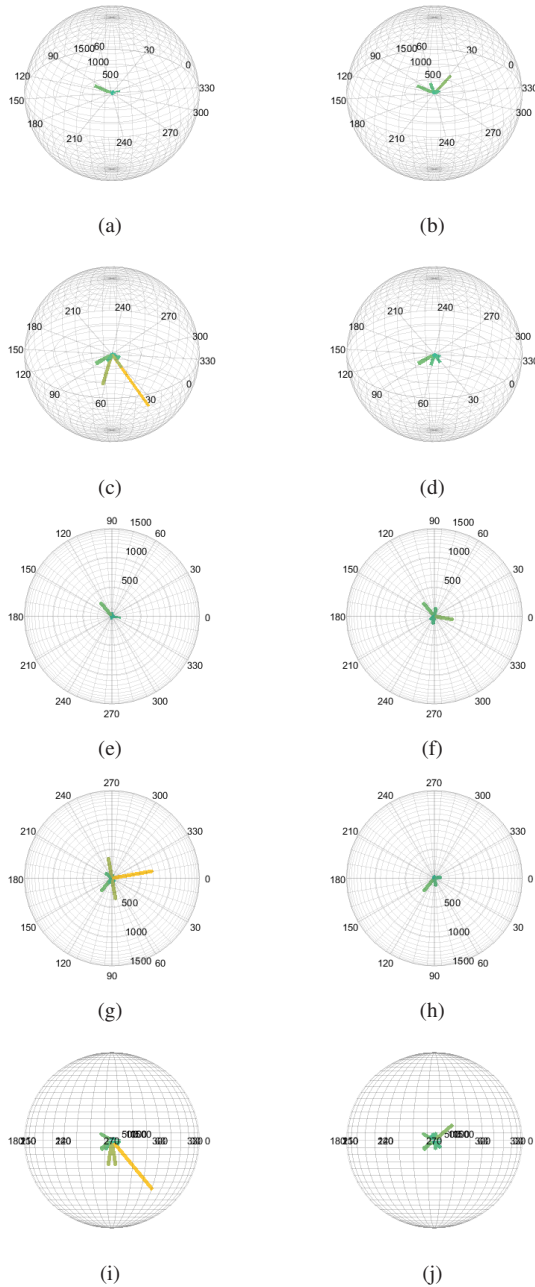
Figure 9. 3D spherical histograms of motion vectors using time volume 30 as the moving volume and time volume 29 as the reference volume. (a) histogram of original volume in the view from top, (b) histogram of registered volume in the view from top, (c) histogram of original volume in the view from bottom, (d) histogram of registered volume in the view from bottom, (e) histogram of original volume in +XY view, (f) histogram of registered volume in +XY view, (g) histogram of original volume in -XY view, (h) histogram of registered volume in -XY view, (i) histogram of original volume in XZ view, (j) histogram of registered volume in XZ view.

its uses in segmentation and annotation," *IEEE Signal Processing Magazine*, vol. 32, no. 1, pp. 70–77, January 2015.

[7] B. Zitova and J. Flusser, "Image registration methods: a survey," *Image and vision computing*, vol. 21, no. 11, pp. 977–1000, June 2003.

[8] P. Matula, M. Kozubek, and V. Dvorak, "Fast point-based 3-D alignment of live cells," *IEEE Transactions on Image Processing*, vol. 15, no. 8, pp. 2388–2396, August 2006.

[9] S. Chang, F. Cheng, W. Hsu, and G. Wu, "Fast algorithm for point pattern matching: Invariant to translations rotations and scale changes," *Pattern Recognition*, vol. 30, no. 2, pp. 311–320, February 1997.

[10] K. Mkrtchyan, A. Chakraborty, and A. Roy-Chowdhury, "Optimal landmark selection for registration of 4D confocal image stacks in arabidopsis," *To appear, IEEE/ACM Transactions on Computational Biology and Bioinformatics*, 2016.

[11] A. Myronenko and X. Song, "Intensity-based image registration by minimizing residual complexity," *IEEE Transactions on Medical Imaging*, vol. 29, no. 11, pp. 1882–1891, June 2010.

[12] G. P. Penney, J. Weese, J. A. Little, P. Desmedt, D. L. G. Hill, and D. J. hawkes, "A comparison of similarity measures for use in 2-D-3-D medical image registration," *IEEE Transactions on Medical Imaging*, vol. 17, no. 4, pp. 586–595, August 1998.

[13] F. Maes, A. Collignon, D. Vandermeulen, G. Marchal, and P. Suetens, "Multimodality image registration by maximization of mutual information," *IEEE Transactions on Medical Imaging*, vol. 16, no. 2, pp. 187–198, April 1997.

[14] P. Thevenaz, U. E. Ruttimann, and M. Unser, "A pyramid approach to subpixel registration based on intensity," *IEEE Transactions on Image Processing*, vol. 7, no. 1, pp. 27–41, January 1998.

[15] S. Yang, D. Kohler, K. Teller, T. Cremer, P. L. Baccon, E. Heard, R. Eils, and K. Rohr, "Nonrigid registration of 3-D multichannel microscopy images of cell nuclei," *IEEE Transactions on Image Processing*, vol. 17, no. 4, pp. 493–499, April 2008.

[16] C. A. Wilson and J. A. Theriot, "A correlation-based approach to calculate rotation and translation of moving cells," *IEEE Transactions on Image Processing*, vol. 15, no. 7, pp. 1939–1951, July 2006.

[17] I. H. Kim, Y. C. M. Chen, D. L. Spector, R. Eils, and K. Rohr, "Nonrigid registration of 2-D and 3-D dynamic cell nuclei images for improved classification of subcellular particle motion," *IEEE Transactions on Image Processing*, vol. 20, no. 4, pp. 1011–1022, September 2010.

[18] T. Du and M. Wasser, "3D image stack reconstruction in live cell microscopy of Drosophila muscles and its validation," *Cytometry Part A*, vol. 75, no. 4, pp. 329–343, April 2009.

[19] R. G. Keys, "Cubic convolution interpolation for digital image processing," *IEEE Transactions on Acoustics, Speech and Signal Processing*, vol. 29, no. 6, pp. 1153–1160, December 1981.

[20] K. S. Lorenz, P. Salama, K. W. Dunn, and E. J. Delp, "Digital correction of motion artifacts in microscopy image sequences collected from living animals using rigid and nonrigid registration," *Journal of Microscopy*, vol. 245, no. 2, pp. 148–160, February 2012.

[21] K. W. Dunn, K. S. Lorenz, P. Salama, and E. J. Delp, "IMART software for correction of motion artifacts in images collected in intravital microscopy," *IntraVital*, vol. 3, no. 1, pp. e28 210:1–10, February 2014.

[22] D. C. Liu and J. Nocedal, "On the limited memory BFGS method for large scale optimization," *Mathematical Programming*, vol. 45, no. 1, pp. 503–528, August 1989.

[23] C. G. Broyden, "The convergence of a class of double-rank minimization algorithms," *IMA Journal of Applied Mathematics*, vol. 6, no. 1, pp. 76–90, 1970.

[24] R. Fletcher, "A new approach to variable metric algorithms," *The Computer Journal*, vol. 13, no. 3, pp. 317–322, 1970.

[25] D. Goldfarb, "A family of variable-metric methods derived by variational means," *Mathematics of Computation*, vol. 24, no. 109, pp. 23–26, January 1970.

[26] D. F. Shanno, "Conditioning of quasi-Newton methods for function minimization," *Mathematics of Computation*, vol. 24, no. 111, pp. 647–656, July 1970.

[27] B. Schmid, J. Schindelin, A. Cardona, M. Longair, and M. Heisenberg, "A high-level 3D visualization API for Java and ImageJ," *BMC Bioinformatics*, vol. 11, no. 274, May 2010.